Carbon 95 (2015) 434–441

Contents lists available at ScienceDirect

Carbon

journal homepage: www.elsevier.com/locate/carbon

Ultralight carbon nanofoam from naphtalene-mediated hydrothermal sucrose carbonization

Shelby Taylor Mitchell [a], Natalie Frese [b], Armin Gölzhäuser [b], Amanda Bowers [a], Klaus Sattler [a, *]

[a] Department of Physics and Astronomy, University of Hawaii, 2505 Correa Road, Honolulu, HI 96822, USA
[b] Faculty of Physics, University of Bielefeld, D-33501 Bielefeld, Germany

ARTICLE INFO

Article history:
Received 5 May 2015
Received in revised form
27 July 2015
Accepted 2 August 2015
Available online 7 August 2015

ABSTRACT

We report experimental studies of carbon nanofoam produced using a hydrothermal autoclave reactor with a sucrose solution and a small added amount of naphthalene. The foam has an average density of 85 mg/cc and is uniform in its appearance. He-ion microscopy (HeIM), Raman spectroscopy and X-ray photoelectron spectroscopy (XPS) were used to characterize the foam samples. These show good consistency in the micro/nanostructure as well as in the elemental constitution. The vibrational and electron core-level studies suggest an open cellular structure with curved graphene walls and basal-plane oxide groups. We conclude that naphthalene-assisted hydrothermal processing of sucrose is a useful method to produce high-quality carbon nanofoams.

1. . Introduction

Nanofoams from various materials have been synthesized in recent years. Among these are nanofoams from chemical elements such as copper [1], silicon [2], nickel [3], gold [4], and silica [5]. Also, various types of polymeric nanofoams have been produced since their first synthesis in 1994 [6]. In addition, nanocomposite foams have been investigated [7] which are interesting due to their superior mechanical and thermal properties. Cu-nanofoams were studied with respect to their possible use in energy applications [1].

There is an intense interest in nanocarbon for a variety of engineering applications. Nanocarbon materials are thermodynamically stable in different polymorphs which can adopt a wide range of crystalline and non-crystalline structures with very interesting properties. This is because of carbon's ability to form sp^1- (polymeric-type), sp^2- (graphite-like), and sp^3- (diamond-like) hybridized bonds. Noncrystalline carbons usually are intermediate between diamond and graphite since they contain variable amounts of sp^3-and sp^2–type atoms. Hybrid graphite-diamond structures have been theoretically developed [8], in particular for the understanding of glassy carbons, carbon blacks, and diamond-like carbon films [9]. The properties of these materials depend very strongly on the sp^3/sp^2 ratio [10]. Mass densities typically range from ~3.5 gcm^{-3} for diamond to about 1 gcm^{-3} for noncrystalline carbon films.

Carbon nanofoam (CNFM) was first produced in 2002 by high-repetition-rate laser ablation of a glassy carbon target in an Argon atmosphere [11]. The foams were found to have very low densities and high electrical resistivity. Carbon nanofoam has been considered as a potential hydrogen storage material [12] and as cathode materials for metal-air batteries [13]. It was found that this material contains both sp^2 and sp^3 bonded carbon atoms. It was suggested that the foams consist of graphite-like sheets with hyperbolic curvature, similar to the structure of “schwarzite”. Surprisingly, ferromagnetism was found for some of the foams up to 90 K, with a narrow hysteresis curve and a high saturation magnetization [14]. Also, catalytic applications have been reported using carbon nanofoams [15]. Atomistic simulations of carbon nanofoams reveal a low-density nanoporous material [16]. A nanofoam-related structure has also been suggested for carbon nanotube aerogels [17]. Such carbon structures with complex topology related to the coexistence of both sp^2 and sp^3 hybridized atoms, have attracted considerable interest in recent years [18].

Porous carbon materials are usually produced by chemical [19,20] or physical [21] routes. Among these, the mesoporous and nanoporous carbons are attractive materials for a number of different applications, such as methane gas storage [22], hydrogen storage [23], as electrodes in supercapacitors [24,25], and as

* Corresponding author.
E-mail address: sattler@hawaii.edu (K. Sattler).

http://dx.doi.org/10.1016/j.carbon.2015.08.001
0008-6223/

matrixes incorporating metal particles for highly efficient catalysts [26,27]. Porous carbon frameworks are also considered for capacitive deionization [28], as sensors for metal ions [29] or as hosts for the confinement of molecules [30].

In this work we report on the study of carbon nanofoams produced by hydrothermal processing of sucrose. Hydrothermal carbonization (HTC), most often applied to biomass processing [31], is an aqueous-phase route to produce carbon materials. High temperature/high pressure (HTHP) synthesis has been shown to lead to the production of a variety of carbon nanomaterials [32]. Separation of carbon species in structural and chemical pure form is usually required but is often difficult to achieve. Our method of hydrothermal processing reveals samples with uniform microstructure as recorded by helium ion microscopy (HeIM). Raman spectra show the typical carbon G and D peaks, no structure in the 2D and 2G overtone range, but two peaks in the 700–1200 cm^{-1} range. The deconvoluted XPS spectra show three C1s peaks which we assign to sp^2/sp^3 hybrid, C–OH, and C=O positioned carbon atoms. In the O1s energy range, we identify three spectral features, corresponding to oxygen bonded to aromatic (sp^2), aliphatic (sp^3), and to carbon atoms in C=O bonds, with the latter presumably from oxygen attached to carbons to the graphene-type basal-plane of the cellular walls.

2. Instruments and methods

2.1. Hydrothermal synthesis

A 130 ml stainless steel autoclave was filled with a 5-molar sucrose solution, and 3 mg of naphthalene was added. The autoclave then was tightly sealed and connected to the heating supply. Subsequently the autoclave was kept at 155 °C for 5 h. After cooling and opening, we extracted the foam which had formed in the container. Then we separated the foam from the remaining sucrose solution by rinsing the samples in hot water. After drying the samples, their mass density was determined using a high-precision balance and a pre-defined volume container. The density was determined for several samples from the same experimental run. The determined value gives an average of three measurements with a standard deviation of 0.8%.

2.2. Helium ion microscopy

Helium ion microscopy images were obtained using the ORION PLUS (Carl Zeiss) with an acceleration voltage of 34.9 eV and a beam current of 0.6 pA. Secondary electrons were detected and an electron flood gun was used to compensate charging of the uncoated samples. The foam was attached to the HeIM sample holder using conductive carbon pads.

The helium ion microscope is a powerful instrument for structure research [33]. It produces a high-brightness, low-energy-spread, subnanometer-size beam for imaging. A beam of He ions with a diameter of typically less than one atom is focused onto the substrate under investigation and the image is provided either by ionoluminescence [34], Rutherford backscattering of the ions, or secondary electron emission [35]. The high resolution is possible due to the small subsurface ion beam spread [36]. Due to its very high brightness it is particularly suitable for the imaging of low-mass elements such as carbon. Besides imaging, elemental analysis can be achieved with the He-ion microscope [37]. In this work we use the secondary electron emission setup for imaging of our samples.

2.3. Raman spectroscopy

Raman spectra were recorded using a micro Raman spectrometer (LabRAM ARAMIS) operated in the backscattering mode. Measurements were performed with a blue diode laser at 473 nm, a 10× microscope objective and a thermoelectrically cooled CCD detector. The foam was mounted on conductive carbon tape.

In Raman spectroscopy, vibrational modes are studied by measuring the energy of photons scattered from a sample which is exposed to laser light. Raman spectra of bulk carbon materials typically consist of a graphitic or G-band, and disorder from defects and from the surface results in the D-band. By determining the ratio between these two bands (I_D:I_G), a quantitative measure of defect density can be obtained. In addition, this intensity ratio can be used to determine the degree of graphitization of a sample.

2.4. X-ray photoelectron spectroscopy (XPS)

X-ray photoelectron spectroscopy was performed in a multichamber UHV system (Multiprobe, Omicron) at a chamber pressure below 10^{-9} mbar. Monochromatic Al Kα irradiation, an electron analyzer (Sphera) with a resolution of 0.9 eV, and an emission angle of 20° were used. The foam was attached to the XPS sample holder by conductive carbon tape. For deconvolution of XP peaks a Shirley background and symmetric Voigt functions were employed.

XPS measures surface composition by determining the binding energy of photoelectrons ejected when a material is irradiated by X-rays. The surface sensitivity of XPS is derived from the small (<10 nm) inelastic mean free path of the ejected photoelectrons. This allows the elemental composition of the near surface region to be quantified.

In addition to compositional analysis, XPS can also provide information on the chemical environment of atoms based on the peak-fitting of the spectral envelopes. This capability stems from the fact that, although a photoelectron's binding energy is largely determined by the element from which it originates, binding energies are also influenced by the local chemical environment (e.g., for carbon atom: C–C, C=C, C–O, C=O).

XPS has been used for a large variety of carbon materials, such as nanostructured carbon films [38], carbon nanowall films [39], diamond-like carbon films [40], amorphous carbon [41], tetrahedral amorphous carbon films [42], nanoporous carbon [43], carbon black [44], activated carbon [45], or carbon nanotubes [46]. The XPS is an excellent instrument for chemical structure analysis [47], in particular for the study of the chemical states with emphasis on the sp^2/sp^3 hybridization ratio [41].

3. Results

3.1. Density

The density of the foam was obtained from averaging the data using various foam samples of the same batch. This resulted in an average density of 0.085 g cm^{-3}. This value is distinctively below the densities of diamond (3.515 g cm^{-3}), graphite (2.267 g cm^{-3}), amorphous carbon (1.8–2.1 g cm^{-3}), or carbon nanotubes (1.6 g cm^{-3}) [48].

Various types of 'ultralight carbons' have been fabricated with densities typically between 100 and 300 mg cm^{-3}. Among these are carbon aerogels [49–51], nanoporous carbons [52], amorphous carbon nanoparticles [53,54], carbon nanotube scaffolds [55], and carbon foams [56,57]. The densities of these carbon materials are significantly different from 'heavy carbons' such as pristine graphite (2.26 g cm^{-3}), DVD grown carbon films (2.14 g cm^{-3} [58]), or carbon nanotube forests (1.6–0.38 g cm^{-3} [59]). Some

techniques allow the production of carbons in a wide density range (0.20–1.4 g cm^{-3} [60]).

3.2. Microscopy

Fig. 1a shows a He-ion microscopy image of a foam sample with a 2 mm field of view. It can be seen that the structure of the material is quite uniform, at this level of magnification. Fig. 1b shows an image of the sample with a 75 micron-sized field of view. At this level of magnification, the sample consists of particles with diameters between ~3 and 15 microns. The particles tend to be spherical, with an eccentricity close to zero, but are often coalesced forming larger species. In Fig. 1c, one of the micropearls is shown enlarged, with a 15 micron field of view. It has a perfectly spherical shape with a sharp edge. On this recorded length scale, the surface of the pearl shows perfectly smooth appearance. However, with further magnification and refocusing of the He ion beam (Fig. 1d, with 1 micron field of view), additional structure can be observed with features as small as ~25 nm in diameter. This may be the diameter of the cavities in the cellular structure of the foam. However, HeIM does not seem to resolve fully the individual pores of the foam. In this respect we note that pore sizes for nanoporous carbons are typically between 0.5 nm and 2 nm [61].

3.3. Raman spectroscopy

Raman spectroscopy is a powerful technique for the characterization of carbon nanomaterials and can be used to distinguish between ordered and disordered atomic structure. The typical features for carbon in Raman spectra are the G band at wavenumbers around 1580 cm^{-1} and the D band at around 1350 cm^{-1}. The G band is usually assigned to E_{2g} phonons of C sp^2 atoms, and the D band is due to the breathing mode of k-point phonons of A_{1g} symmetry [62]. The G band may also contain signatures from polycyclic aromatic hydrocarbons (PAHs), often the precursors in the growth of graphitic particles [63]. Carbon stretch vibrations in benzene result in a peak at 1588 cm^{-1} [64], and PAH signatures are at similar wavenumbers.

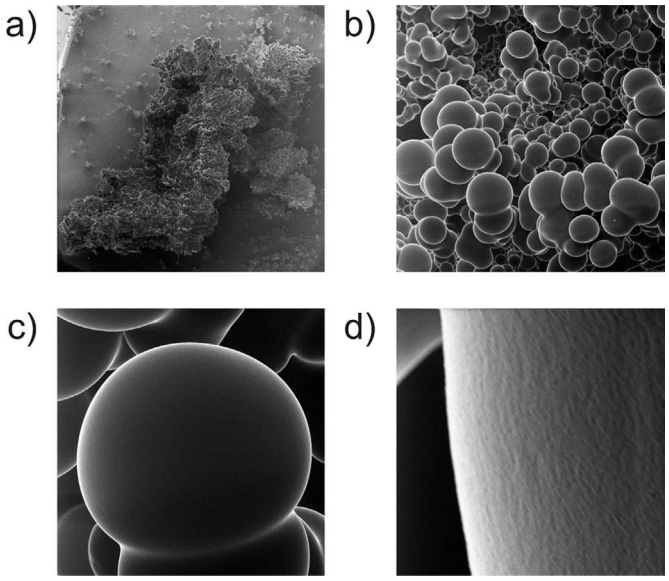

Fig. 1. Helium-ion microscopy (HeIM) images of carbon nanofoam, Fields of view: (a) 2 mm, (b) 75 μm, (c) 15 μm, showing a single micropearl, and (d) 1 μm, showing a micropearl with internal structure.

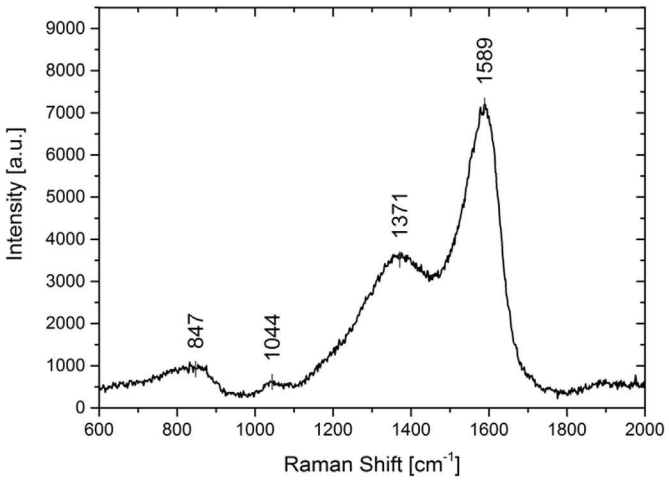

Fig. 2. Raman spectrum in the wavenumber range 750 cm^{-1} to 2300 cm^{-1}.

Fig. 2 shows the Raman spectrum of our foam sample. We identify the two characteristic peaks, the G band at 1589 cm^{-1} and the D band at 1371 cm^{-1}. The G band appears with much higher intensity than the D band. Such intense G band indicates the significant presence of a graphitic wall structure, presumably with single- or few-layer thickness. The wavenumber of the observed G band (1589 cm^{-1}) is slightly shifted to a higher value compared to that of the graphite G band (1580 cm^{-1}), which may result from high curvature of a graphene wall structure. The relatively low D-band intensity indicates that the nanofoam samples contain few carbons in hybridizations other than sp^2. We further note that the overtone of the D band, the 2D band, is usually located at about 2700 cm^{-1} [65]. In our sample, the 2D band is not present in the extended spectrum.

3.4. XPS

XPS is a powerful method to investigate the character of the near-surface region of carbonaceous materials. It is a surface sensitive method in which the core level chemical shifts are measured. This is valuable for understanding the local environment of an atom, for example in finding whether a carbon allotrope is sp^3 or sp^2 bonded. Apart from the chemical shift, the XPS investigation can provide useful information such as elemental composition, degree of disorder, compound formation, and surface functional groups.

Using XPS, the identity and concentration of oxygen-containing functional groups can, in principle, be obtained from spectral deconvolution of the C1s and O1s XPS regions. Unambiguous spectral deconvolution is, however, often complicated by the presence of different species (e.g., C–H, C–O, C=O, COOH) with similar binding energies. The C1s and the O1s spectral envelopes are typically broad and featureless due to both the proximity of the binding energies associated with different oxygen-containing functional groups and the limited resolution of typical energy analyzers.

In Fig. 3a and b, narrow-scan XPS spectra are provided for the C1s and O1s peak distributions, respectively. The two energy ranges cover the typical features present in the analysis of nanocarbon materials.

For the distribution in Fig. 3a we used three-curve fitting. We label the three peaks as C1, C2 and C3, and find the maxima and % areas at 285.0 eV (57.0%), 286.2 eV (32.0%), and 288.6 eV (11.0%), respectively. We assign the C1 peak to C–C bonds in a mixed sp^2/

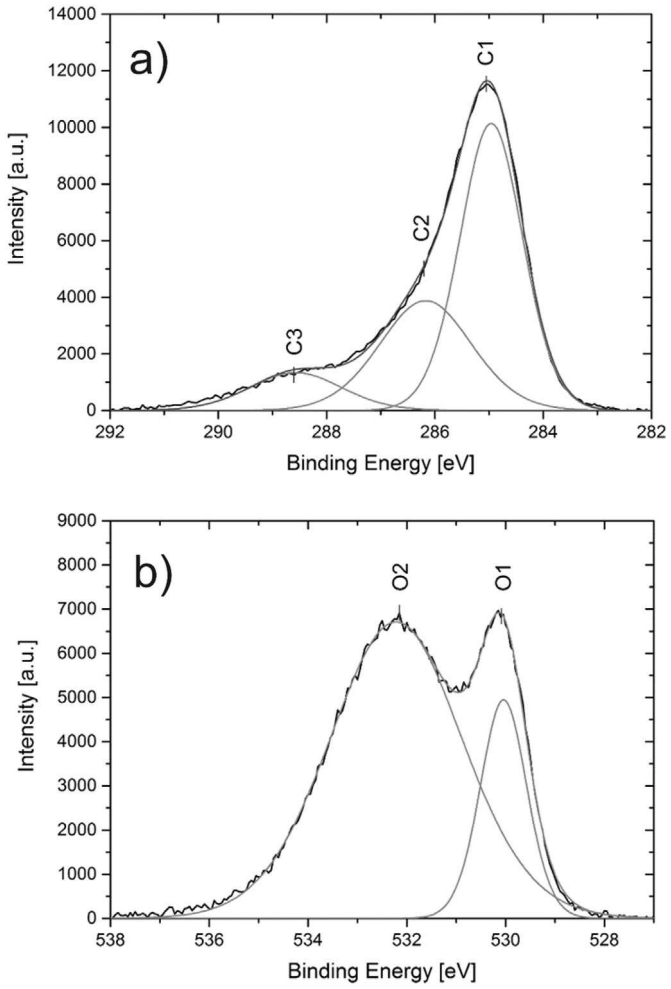

Fig. 3. XPS spectra showing the spectral regions of (a) C1s atomic carbon orbitals, and (b) O1s atomic oxygen orbitals.

sp^3 hybridization state since this peak is located between the graphite-type peak at about 284.3 eV and the diamond peak at about 285.5 eV. The C1 peak, with 57.0% area, gives the dominant contribution to the C1s region. The C2 and C3 peaks are assigned to carbon atoms in C–O and C=O bond configurations, respectively. The C–O peak has about half the area of the C–C peak, and the C=O peak a much smaller fraction.

The spectrum in Fig. 3b gives the distribution of the O1s core level energy with the oxygen atom in different bond environments. Application of two fitting curves gives the best results. Two peaks are identified, at 530.0 eV (O1) and at 532.2 eV (O2) with areas of 20.6% and 79.4%, respectively. We assign the broad peak, at 532.2 eV, to carbons in C–O bonds at sp^2 and sp^3 hybridized carbons, i.e. with the carbon atoms located in a diamond-graphite hybrid environment. The fact, that both, sp^2-and sp^3-related peaks are not separated in the O1s distribution suggests that there is no phase separation between sp^2 and sp^3 regions in the sample, a result which we also had obtain considering the location of the C1s C–C peak at 285.0 eV.

It has been reported that oxygen atoms in carbon materials with adsorbed water yield a peak in the 536–537 eV range (536 eV [96], 537.1 eV [66]). Since no such peak is found in our XPS spectrum, we conclude that the water from the sucrose/naphthalene solution has been completely extracted in drying the samples.

4. Discussion

We first discuss the Raman results. We find for our foam sample that the D and G bands are distinctively separated, different from the broad distribution of one unresolved peak observed for amorphous carbon [67]. This reveals that the foams have an ordered atomic structure.

In a survey, values for the G-band position between ~1554 cm^{-1} and ~1595 cm^{-1} have been given for a range of graphene-, nanotube-, and fullerene-type carbon allotropes [68]. The G peak is positioned at 1581 cm^{-1} [68] in pristine graphite. However, it is usually shifted to higher values for the various nanocarbon materials. It was, for example, detected at 1593 cm^{-1} for carbon nanopearls [69], at 1591 cm^{-1} for carbon nanospheres [70] and 1595 cm^{-1} for graphene nanosheets [71]. The upshift of the Raman band has been attributed to highly-curved structures and small sizes of carbon species [68]. In our study of the carbon nanofoams we find the G band at 1589 cm^{-1}, which suggests that the nanofoam has a wall structure composed of curved graphene walls.

Numerous studies have shown that the D-band lies at ~1350 cm^{-1} and is quite insensitive to the type of nanocarbons considered. I has been located at this value for porous carbon scaffolds (1350 cm^{-1}, [72]), disordered nanocarbons (1350 cm^{-1}, [73]), nanopearls (1350 cm^{-1}, [69]), carbon nanotubes (1349 cm^{-1}, [74]), and others. It was found at slightly higher values (1358 cm^{-1}, [75]) for cluster-assembled carbons, and at a lower value (1337 cm^{-1}, [70]) for carbon nanospheres. For the nanofoam sample in this study we find a value of 1371 cm^{-1} for the D band position which is consistent with the nanoporous structure of the foam having a curved and strained wall structure.

The characteristic Raman band has been observed at ~1332 cm^{-1} for diamond films [76] and for nanocrystalline diamond [77]. In the case of phase separation, separate diamond and graphite areas would be present in the foam. However, no corresponding feature is found in the foam spectrum. We conclude that no indication for a phase separation of sp^2 and sp^3 regions is found.

We note that our foam samples show some structure in the Raman spectrum for wave numbers ~1850–2140 cm^{-1}, the range where features due to carbon chains are usually observed [73]. In this wavenumber range one expects a band originating from vibrations of carbon triple bonds, associated with the presence of conjugated polyacetylenic bonds with a distribution of chain lengths. The slightly enhanced intensity for wavenumbers ~1850–2140 cm^{-1}, displayed in Fig. 2, indicates that carbon triple bonds are included in the cell structure of the foam.

We don't have any indication for a 2D peak in our sample; if present, its intensity is below the noise level. The 2D band, located near 2700 cm^{-1}, gives a very strong peak for pristine graphene. However it is substantially reduced in finite graphene nanosheets [78]. Also, its intensity is sensitive to the degree of order in the sample. When exposed to Ar^+-ion bombardment, this band significantly decreases, as shown in a study where the distance between ion impact-produced point defects was changed from 24 nm to 2 nm [79]. This reveals, that increasing degree of disorder leads to a suppression of the 2D band. Therefore, this band is usually not present in defective carbons such as graphene oxide and graphene aerogels [80]. Another property influencing the occurrence and height of the 2D peak is the curvature of the graphene network. It has been shown that the 2D peak becomes significantly lower when the diameter of a nanotube is reduced from 20 nm to 3 nm [81]. These results indicate that the nanofoams in our study have a strongly-curved defective graphene-type wall structure.

The nanofoam samples show features in the Raman spectrum in the wavenumber range of 800–1100 cm^{-1}, as seen in Fig. 2 at

847.5 cm^{-1} and 1043.9 cm^{-1}. Two peaks in this range, at 860 cm^{-1} and 1100 cm^{-1}, have previously been observed for carbon onions [82]. A 1150 cm^{-1} mode has also been found for nanocrystalline diamond [83]. A peak at 1190 cm^{-1} was observed for amorphous hydrogenated carbon films produced by plasma deposition [84]. We conclude that our observed band at 847.5 cm^{-1} may originate from structures similar to carbon onions. The 1043.9 cm^{-1} band is well below the band for nanocrystalline diamond. Therefore there is no indication for a diamond-graphite phase separation in our samples.

Five bands characterize the Raman spectrum of naphthalene ($C_{10}H_8$); at 513.8 cm^{-1}, 763.8 cm^{-1}, 1021.6 cm^{-1}, 1382.2 cm^{-1}, and 1464.5 cm^{-1} [85]. The Raman spectrum of our foam sample does not show any sharp peaks at these wave numbers which points to complete carbonization of the naphthalene in the hydrothermal process of the sucrose/naphthalene solution.

Next we discuss the XPS results. Deconvolution of the C1s envelope for the nanofoams yields three peaks, labeled as C1, C2, and C3 in Fig. 3a. We attribute the C1 component to C—C bonds, the C2 and C3 peaks to C—O and C═O bonds, respectively.

We consider the location of the C1 core line. There is a general agreement (within +/− 0.2 eV) about the binding energy of 284.3 eV for the 1s electron of a carbon atom in pristine graphite [86]. This binding energy is also found for a variety of C-based materials such as graphite oxide [87], multiwall carbon nanotubes [88], amorphous carbon films [89], carbon blacks [66], thin films of C_{60} [90], graphene [91], graphene oxide [92], and others. The location of this peak has been shown to be quite insensitive to strong changes in the carbon material's crystalline order. It was found, that with intense Ar^+ ion radiation of highly-oriented pyrolytic graphite (HOPG), the position of the C1 peak remained almost unchanged while the width (FWHM) changed significantly, from 0.6 eV to 1.5 eV [93]. Yet, small shifts to higher binding energies of 284.6 eV [94], 284.7 eV [95], and 284.8 eV [96] have been observed for various graphene oxide materials. In our studies of carbon nanofoams we also find an upward shift of the binding energy and observe the C—C peak at 284.96 eV. This indicates that the cellular walls of the foam in this study have structures related to graphene oxide.

This shift in binding energy may be explained by the presence of highly-curved and strained graphene walls in the foam structure. In fact, a value of 284.92 eV has been observed for strongly-curved single-wall carbon nanotubes [88]. The observed peak position is slightly below the sp^3-originated C1s peak, which was found in the range of 285.2 eV–285.8 eV for diamond [97], hydrogenated amorphous carbon films [89], CVD diamond [89], and other diamond-like structures [98]. Therefore we suggest that the foam sample is characterized by a hybrid sp^2-sp^3 structure of cavities with curved graphene sidewalls and with sp^3 bonds providing the links for the 3-dimensional graphene-like network. Hybrid graphene-diamond structures have been previously suggested by several research groups, with respect to their structural [99,100] and electronic [8] properties, and to their phase stability [101].

Another area of discussion is the width of the observed XPS peaks. For highly oriented pyrolytic graphite (HOPG) the crystals have close-to perfect atomic structures and the C1s peak is narrow, with a FWHM of 0.45 eV [93]. In defect-free graphite the electronic environment is the same for all carbon atoms. Consequently, the XPS spectrum of HOPG shows a narrow peak. The width of the peak is related to the heterogeneity of the electronic environment of the carbon atoms. Differences in the nearest-neighbor configuration will slightly shift the binding energy and cause a broadening of the observed peak. For the foam sample we determine a full-width at half maximum (FWHM) of 1.4 eV. We explain this by the heterogeneity of the hybrid structure containing sp^2-and sp^3-type carbon atoms without a major phase separation.

The C2 peak in the C1s distribution, at 286.2 eV, has an area of 32.0%. It has been assigned to C—OH bonds in a number of studies of graphene oxide with reported values of 286.4 eV [102] and 286.2 eV [96]. It is typically found in the range of 285.5 eV–287.5 eV with carbon samples prepared under various conditions [103]. The peak receives its relatively large width from the coexistence of carbons in sp^2 and sp^3 configurations.

The C3 peak, at 288.6 eV, has a relative area of 11.0% and can be associated with C═O and carboxyl (COOH) groups [98,99]. These two functional groups usually are strong features in graphene oxide [104]. The C3 peak in our sample is well below the peaks at 290.6 eV and 291.6 eV usually assigned to shake-up satellite ($\pi \rightarrow \pi^*$) and plasmon excitations, respectively [105]. In shake-up events the emission process is accompanied by the promotion of an electron in one of the highest occupied orbitals into one of the lowest unoccupied orbitals. This leads to a photoelectron emitted from the solid with lower kinetic energy and the appearance of a higher binding energy for the C1s state. The lack of a plasmon excitation feature shows the insulating character of the foam sample. Both excitations, characteristic for HOPG, do not appear to be present in our foam sample or are too weak to give a measurable signal in the XPS spectrum. In fact, these features, related to the perfect crystal structure of HOPG, disappear when HOPG is exposed to Ar^+ ion radiation, i.e. with increasing degree of disorder [86].

One of the main objectives in the synthesis of new carbon materials is to find allotropes composed of carbon atoms in combined hybridized states, such as sp-sp^3, sp^2-sp^3, or sp-sp^2-sp^3. Also, carbon atoms may exist in intermediate states sp^n, where n is a fractional number, with $1 < n < 2$ for cyclo(N)carbons and $2 < n < 3$ for closed-frame structures [106]. On the other hand, two phases may coexist side by side in different areas of a sample. For example, self-formed C_{60} inclusions were found in hydrogenated carbon films [107]. In this respect, it is interesting to ask if there is phase separation between different hybridizations in the foam sample. For example, clusters of sp^3-bonded carbons could be incorporated in a graphitic framework. If nanodiamond-type clusters were constituents of the sample, one should observe a narrow C1s peak according to these species. The 1s core level peak of pristine nanodiamonds was observed at 289.07 eV [108], which is about 3 eV above the sp^3 peak in bulk diamond. Since no such peak is seen in our XPS spectra, we can exclude that nanodiamond areas are part of the foam structure. The spectra rather indicate that the foam scaffold is made of mixed sp^2/sp^3 bonding in a graphite-diamond hybrid network.

Information provided by analysis of the O1s spectra can complement the information from the analysis of C1s spectra. We note that, because the O1s photoelectron kinetic energies are lower than those of the C1s, the O1s sampling depth is smaller, and therefore the O1s spectra are slightly more surface specific.

In Fig. 3b we display the O1s binding energy distribution in the 525 eV–545 eV region. The spectrum shows two main features; a broad peak with relative peak area of 79.4% centered at 532.2 eV and a narrow peak centered at 530.0 eV with 20.6 area%. The observed maxima are very close to those found for oxygen-treated carbon materials [109]. A peak at ~533 eV is usually assigned to oxygen atoms bonded to carbon through aromatic sp^2 orbitals. A peak at ~531 eV is usually attributed to oxygen bonded to carbon through aliphatic sp^3 orbitals. The assumption of the coexistence of two different oxygen functionalities in our sample is supported by the very broad O1s peak at 532.2 eV, with a FWHM of about 3 eV.

The O1 peak, at 530.0 eV, is narrow and rarely seen in carbon nanomaterials. However, it was observed in the studies of a single layer graphene on Cu foil [110] with oxygen atoms adsorbed to the

surface of the layer. In another study, this peak was found at 530.6 eV for graphene oxide and was assigned to oxygen atoms in C═O bonds [111]. It is commonly observed, that the basal plane of graphene in graphene oxide is functionalized mostly with epoxide and hydroxyl groups, and the edges with carbonyl and carboxyl groups. Therefore, for the foam samples in this study, we ascribe the peak at 530.0 eV to oxygen atoms bonded to the basal plane of graphene oxide walls forming the cavities of the nanoporous foam structure.

We note that the type of oxygen functionalities present at the carbon surface affects the electrochemical response of the carbon material. It has been found that microporous carbon materials cannot be fully wetted in aqueous solutions because of their hydrophobic character [112]. Higher oxygen content affects the electric field in the surface by changing local polarity, which leads to an increase of the interaction with water molecules [61]. The prospects of future applications of carbon nanofoams may depend on the type of oxygen functionalization in the foams, and basal-plane-attached oxygen atoms may play a significant role in determining the electrochemical properties.

It is not possible to directly determine if the micropearls seen in the images of Fig. 1b are hollow with a thin graphite skin or if they are solid with a cellular structure of cavities on the nanometer scale. Both topologies could describe the ultralow density of the foam. However, since we don't observe any water or sucrose signatures in Raman and XPS spectra, the cellular structure with open channels to the periphery of the foam seems to better describe the foam morphology. These structures presumably have on the nanoscale the topology of "negative-curvature" carbons (NCCs) with graphene-thin walls, similar to 'schwartzites', with sp^2 and sp^3 carbons forming an aperiodic space structure. N-gons larger than hexagons may also contribute to the curved graphitic structure [113]. Basal-plane hydrogenation and oxidation of the graphene wall leads to out-of-plane corrugation and strain, as found in materials such as graphene oxide and graphane [114]. Similar structures seem to describe the walls of the nanofoams in this study.

5. Conclusion

We have shown with our investigations that a small amount of naphthalene added to an aqueous sucrose solution, processed in a hydrothermal reactor, leads to the formation of carbon nanofoam. No traces of sucrose and naphthalene are detected in the foam and we conclude that the sucrose/naphthalene solution has completely been carbonized. The obtained foam has a continuous structure and has ultralow mass density. He-ion microscopy studies show an assembly of micron-sized carbon pearls as the structure of the foam on the micrometer length scale. With further magnification, features on as small as ~25 nm are observed. A porous structure on the nanometer length scale is required in order to explain the ultralow density of the foam. Raman and XPS studies of the foam sample reveal the characteristic spectroscopic features of nanocarbons. In addition, detailed analysis shows that signatures from aromatic and aliphatic bonds are not separated but lead to combined peaks. This observation helps to better understand the topologically complex carbon foam structure. It indicates that there is no phase separation between graphite- and diamond-like regions and that the foams are structured as a network of carbons in a hybrid sp^2/sp^3 orbital configuration. Further, the Raman and XPS results suggest that on the nanometer scale the foams appear to be composed of a curved graphene scaffold with oxygen functional groups at the basal-plane of graphene. Neither water, sucrose, or naphthalene signatures are seen in the spectra which suggests that the foam morphology does not contain closed cavities but has channels open to the periphery of the sample. Such an open cellular structure might be useful for future applications of the material as a hydrogen gas or biomedical liquid storage medium.

Acknowledgement

The authors thank Christof Neumann for technical help with the Raman spectrometer.

References

[1] H. Jo, et al., Novel method of powder-based processing of copper nanofoams for their potential use in energy applications, Mater. Chem. Phys. 145 (1–2) (2014) 6–11.
[2] M. Castro, et al., Pattern-wavelength coarsening from topological dynamics in silicon nanofoams, Phys. Rev. Lett. 112 (9) (2014).
[3] Y.J. Fu, et al., Template-free synthesized Ni nanofoams as nanostructured current collectors for high-performance electrodes in lithium ion batteries, J. Mater. Chem. A 1 (34) (2013) 10002–10007.
[4] M. Caro, et al., Radiation induced effects on mechanical properties of nanoporous gold foams, Appl. Phys. Lett. 104 (23) (2014).
[5] A. Kurek, et al., Silica Nanofoam (NF) supported single- and dual-site catalysts for ethylene polymerization with morphology control and tailored bimodal molar mass distributions, Macromolecules 46 (23) (2013) 9197–9201.
[6] S. Jayaraman, et al., High T(G)polyimide nanofoams derived from pyromellitic dianhydride and 1,1-bis(4-aminophenyl)-1-phenyl-2,2,2-trifluromethane, Abstr. Pap. Am. Chem. Soc. 207 (1994), p. 20-POLY.
[7] S. Tabandeh, F.A. Taromi, H. Nazockdast, Flexible polyurethane nanocomposite foam: synthesis and properties, Polym. Sci. Ser. B 56 (5) (2014) 681–685.
[8] F.J. Ribeiro, et al., Structural and electronic properties of carbon in hybrid diamond-graphite structures, Phys. Rev. B 72 (21) (2005).
[9] C.Z. Wang, K.M. Ho, Structure, dynamics, and electronic-properties of diamond-like amorphous-carbon, Phys. Rev. Lett. 71 (8) (1993) 1184–1187.
[10] O.S. Panwar, et al., XPS and XAES studies of as grown and nitrogen incorporated tetrahedral amorphous carbon films deposited by pulsed unfiltered cathodic vacuum arc process, Appl. Surf. Sci. 221 (1–4) (2004) 392–401.
[11] A.V. Rode, et al., Electronic and magnetic properties of carbon nanofoam produced by high-repetition-rate laser ablation, Appl. Surf. Sci. 197 (2002) 644–649.
[12] R. Blinc, et al., Carbon nanofoam as a potential hydrogen storage material, Phys. Status Solidi B Basic Solid State Phys. 244 (11) (2007) 4308–4310.
[13] C.N. Chervin, et al., Carbon nanofoam-based cathodes for Li-O-2 batteries: correlation of pore solid architecture and electrochemical performance, J. Electrochem. Soc. 160 (9) (2013) A1510–A1516.
[14] A.V. Rode, et al., Unconventional magnetism in all-carbon nanofoam, Phys. Rev. B 70 (5) (2004).
[15] J. Garcia-Martinez, T.M. Lancaster, J.Y. Ying, Synthesis and catalytic applications of self-assembled carbon nanofoams, Adv. Mater. 20 (2) (2008) 288–292.
[16] C. Mathioudakis, P.C. Kelires, Atomistic simulations of low-density nanoporous materials: carbon nanofoams, Phys. Rev. B 87 (19) (2013).
[17] S. Charnvanichborikarn, et al., Nanoporous Cu-C composites based on carbon-nanotube aerogels, J. Mater. Chem. A 2 (4) (2014) 962–967.
[18] Z. Zhu, et al., Topologically protected conduction state at carbon foam surfaces: an Ab initio Study, Phys. Rev. Lett. 112 (2) (2014).
[19] B.B. Chang, et al., Synthesis of sulfonated porous carbon nanospheres solid acid by a facile chemical activation route, J. Solid State Chem. 221 (2015) 384–390.
[20] L.Q. Duan, et al., Fabrication and electrochemical performance of nanoporous carbon derived from silicon oxycarbide, Microporous Mesoporous Mater. 202 (2015) 97–105.
[21] S.I. Kim, et al., Making porous conductive carbon films with unbalanced magnetron sputtering, Jpn. J. Appl. Phys. 54 (1) (2015).
[22] X.Y. Zhu, Y.P. Zhao, Atomic mechanisms and equation of state of methane adsorption in carbon nanopores, J. Phys. Chem. C 118 (31) (2014) 17737–17744.
[23] S. Leyva-Garcia, et al., New insights on electrochemical hydrogen storage in nanoporous carbons by in situ Raman spectroscopy, Carbon 69 (2014) 401–408.
[24] R.S. Kalubarme, C.J. Park, P.M. Shirage, Two-dimensional mesoporous carbon electrode for high energy density electrochemical supercapacitors, J. Nanosci. Nanotechnol. 15 (2) (2015) 1253–1260.
[25] J. Yin, et al., Meso- and micro- porous composite carbons derived from humic acid for supercapacitors, Electrochim Acta 136 (2014) 504–512.
[26] L. Zhong, et al., Pd nanoparticles embedded in mesoporous carbon: a highly efficient catalyst for Suzuki-Miyaura reaction, Catal. Today 243 (2015) 195–198.
[27] Y.B. Wang, H.Y. Zhao, G.H. Zhao, Iron-copper bimetallic nanoparticles embedded within ordered mesoporous carbon as effective and stable heterogeneous Fenton catalyst for the degradation of organic contaminants, Appl. Catal. B Environ 164 (2015) 396–406.

[28] Y. Liu, et al., Porous carbon spheres via microwave-assisted synthesis for capacitive deionization, Electrochim Acta 151 (2015) 489–496.
[29] D.L. Xiao, et al., Porous carbon quantum dots: one step green synthesis via L-cysteine and applications in metal ion detection, RSC Adv. 5 (3) (2015) 2039–2046.
[30] F. Barroso-Bujans, et al., Intercalation and confinement of poly(ethylene oxide) in porous carbon nanoparticles with controlled morphologies, Macromolecules 47 (24) (2014) 8729–8737.
[31] K. Tekin, S. Karagoz, S. Bektas, A review of hydrothermal biomass processing, Renew. Sustain. Energy Rev. 40 (2014) 673–687.
[32] A. Bazargan, et al., A review: synthesis of carbon-based nano and micro materials by high temperature and high pressure, Ind Eng. Chem. Res. 52 (36) (2013) 12689–12702.
[33] N.P. Economou, J.A. Notte, W.B. Thompson, The history and development of the helium ion microscope, Scanning 34 (2) (2012) 83–89.
[34] S.A. Boden, et al., Ionoluminescence in the helium ion microscope, Microsc. Microanal. 18 (6) (2012) 1253–1262.
[35] K. Ohya, T. Yamanaka, Modeling secondary electron emission from nanostructured materials in helium ion microscope, Nucl. Instrum. Methods Phys. Res. Sect. B Beam Interact. Mater. Atoms 315 (2013) 295–299.
[36] S. Sijbrandij, et al., Analysis of subsurface beam spread and its impact on the image resolution of the helium ion microscope, J. Vac. Sci. Technol. B 28 (6) (2010). C6F6–C6F9.
[37] S. Sijbrandij, et al., Elemental analysis with the helium ion microscope, J. Vac. Sci. Technol. B 26 (6) (2008) 2103–2106.
[38] P. Kerber, et al., Study of surface cleaning methods and pyrolysis temperatures on nanostructured carbon films using X-ray photoelectron spectroscopy, J. Vac. Sci. Technol. A 30 (6) (2012).
[39] A. Achour, et al., Electrochemical anodic oxidation of nitrogen doped carbon nanowall films: X-ray photoelectron and Micro-Raman spectroscopy study, Appl. Surf. Sci. 273 (2013) 49–57.
[40] M. Tagawaa, et al., Synchrotron radiation photoelectron spectroscopy and near-edge X-ray absorption fine structure study on oxidative etching of diamond-like carbon films by hyperthermal atomic oxygen, Appl. Surf. Sci. 256 (24) (2010) 7678–7683.
[41] R. Haerle, et al., sp(2)/sp(3) hybridization ratio in amorphous carbon from C 1s core-level shifts: X-ray photoelectron spectroscopy and first-principles calculation, Phys. Rev. B 65 (4) (2002).
[42] B.K. Tay, et al., Investigation of tetrahedral amorphous carbon films using X-ray photoelectron and Raman spectroscopy, Surf. Interface Anal 28 (1) (1999) 231–234.
[43] S.K. Gordeev, et al., Study of bonding in nanoporous carbon by X-ray photoelectron spectroscopy, Mol. Mater. 13 (1–4) (2000) 355–360.
[44] M. Manickam, M. Takata, Electrochemical and X-ray photoelectron spectroscopy studies of carbon black as an additive in Li batteries, J. Power Sources 112 (1) (2002) 116–120.
[45] K.V.V. Rao, et al., X-Ray Photoelectron spectroscopy studies on activated carbon prepared from rind of citrus nobilis, Asian J. Chem. 22 (6) (2010) 4377–4381.
[46] S. Oida, F.R. McFeely, A.A. Bol, X-ray photoelectron spectroscopy study on Fe and Co catalysts during the first stages of ethanol chemical vapor deposition for single-walled carbon nanotube growth, J. Appl. Phys. 109 (6) (2011).
[47] S. Takabayashi, et al., Chemical structural analysis of diamondlike carbon films with different electrical resistivities by X-ray photoelectron spectroscopy, Jpn. J. Appl. Phys. 47 (5) (2008) 3376–3379.
[48] D.R. Lide, in: D.R. Lide (Ed.), CRC Handbook of Chemistry and Physics, 86 ed, CRC Press, Baco Raton (FL), 2005.
[49] J.Z. Feng, J. Feng, C.R. Zhang, Thermal conductivity of low density carbon aerogels, J. Porous Mater. 19 (5) (2012) 551–556.
[50] J. Marie, et al., Highly porous PEM fuel cell cathodes based on low density carbon aerogels as Pt-support: Experimental study of the mass-transport losses, J. Power Sources 190 (2) (2009) 423–434.
[51] B. Zhou, et al., Preparation of low density and high mesoporosity carbon aerogels by an organic/inorganic hybrid method, New Carbon Mater. 26 (2) (2011) 117–122.
[52] L.J. Peng, J.R. Morris, Structure and hydrogen adsorption properties of low density nanoporous carbons from simulations, Carbon 50 (3) (2012) 1394–1406.
[53] R.B. dos Santos, F.D. Mota, R. Rivelino, A theoretical evaluation of the effect of water on the electronic properties of low density amorphous carbon nanoparticles, Carbon 50 (8) (2012) 2788–2795.
[54] Y.N. Feng, et al., Pore size controllable preparation for low density porous nano-carbon, J. Nanosci. Nanotechnol. 13 (10) (2013) 7012–7015.
[55] S.J. Shin, et al., Robust nanoporous alumina monoliths by atomic layer deposition on low-density carbon-nanotube scaffolds, Carbon 73 (2014) 443–447.
[56] S. Chaurasia, et al., Laser interaction with low-density carbon foam, Pramana Journal Phys. 75 (6) (2010) 1191–1196.
[57] A. Zani, et al., Ultra-low density carbon foams produced by pulsed laser deposition, Carbon 56 (2013) 358–365.
[58] T. Urakawa, et al., Mass density control of carbon films deposited by H-assisted plasma CVD method, Surf. Coatings Technol. 228 (2013) S15–S18.
[59] H. Sugime, et al., Growth kinetics and growth mechanism of ultrahigh mass density carbon nanotube forests on conductive Ti/Cu supports, ACS Appl. Mater. Interfaces 6 (17) (2014) 15440–15447.
[60] R. Brandt, J. Fricke, Acetic-acid-catalyzed and subcritically dried carbon aerogels with a nanometer-sized structure and a wide density range, J. Non-Cryst. Solids 350 (2004) 131–135.
[61] M.J. Bleda-Martinez, et al., Chemical and electrochemical characterization of porous carbon materials, Carbon 44 (13) (2006) 2642–2651.
[62] A.C. Ferrari, J. Robertson, Interpretation of Raman spectra of disordered and amorphous carbon, Phys. Rev. B 61 (20) (2000) 14095–14107.
[63] H. Hepp, K. Siegmann, K. Sattler, New aspects of growth mechanisms for polycyclic aromatic-hydrocarbons in-diffusion flames, Chem. Phys. Lett. 233 (1–2) (1995) 16–22.
[64] J. Schwan, et al., Tetrahedral amorphous carbon films prepared by magnetron sputtering and dc ion plating, J. Appl. Phys. 79 (3) (1996) 1416–1422.
[65] M. Sarno, et al., A study of the key parameters, including the crucial role of H-2 for uniform graphene growth on Ni foil, J. Mol. Catal. A Chem 366 (2013) 303–314.
[66] D. Pantea, et al., Electrical conductivity of conductive carbon blacks: influence of surface chemistry and topology, Appl. Surf. Sci. 217 (1–4) (2003) 181–193.
[67] M. Chhowalla, et al., Evolution of sp(2) bonding with deposition temperature in tetrahedral amorphous carbon studied by Raman spectroscopy, Appl. Phys. Lett. 76 (11) (2000) 1419–1421.
[68] S. Gupta, A. Saxena, Nanocarbon materials: probing the curvature and topology effects using phonon spectra, J. Raman Spectrosc. 40 (9) (2009) 1127–1137.
[69] C.N. Hunter, et al., Tribological properties of carbon nanopearls synthesized by nickel-catalyzed chemical vapor deposition, Tribol. Lett. 30 (3) (2008) 169–176.
[70] D. Yuan, et al., Preparation of monodisperse carbon nanospheres for electrochemical capacitors, Electrochem. Commun. 10 (7) (2008) 1067–1070.
[71] G. Wang, et al., Facile synthesis and characterization of graphene nanosheets, J. Phys. Chem. C 112 (22) (2008) 8192–8195.
[72] M.T. Johnson, K.T. Faber, Catalytic graphitization of three-dimensional wood-derived porous scaffolds, J. Mater. Res. 26 (1) (2011) 18–25.
[73] M.A. Pimenta, et al., Studying disorder in graphite-based systems by Raman spectroscopy, Phys. Chem. Chem. Phys. 9 (11) (2007) 1276–1291.
[74] L. Ci, R. Vajtai, P.M. Ajayan, Vertically aligned large-diameter double-walled carbon nanotube arrays having ultralow density, J. Phys. Chem. C 111 (26) (2007) 9077–9080.
[75] D. Bolgiaghi, et al., Pulsed laser deposition of glass-like cluster assembled carbon films, Carbon 43 (10) (2005) 2122–2127.
[76] A.A. Zakhidov, et al., Carbon structures with three-dimensional periodicity at optical wavelengths, Science 282 (5390) (1998) 897–901.
[77] J. Birrell, et al., Interpretation of the Raman spectra of ultrananocrystalline diamond, Diam. Relat. Mater. 14 (1) (2005) 86–92.
[78] G.X. Wang, et al., Facile synthesis and characterization of graphene nanosheets, J. Phys. Chem. C 112 (22) (2008) 8192–8195.
[79] L.G. Cancado, et al., Quantifying defects in graphene via Raman spectroscopy at different excitation energies, Nano Lett. 11 (8) (2011) 3190–3196.
[80] M.A. Worsley, et al., High surface area, sp(2)-cross-linked three-dimensional graphene monoliths, J. Phys. Chem. Lett. 2 (8) (2011) 921–925.
[81] E.F. Antunes, et al., Influence of diameter in the Raman spectra of aligned multi-walled carbon nanotubes, Carbon 45 (5) (2007) 913–921.
[82] D. Roy, et al., Characterisation of carbon nano-onions using Raman spectroscopy, Chem. Phys. Lett. 373 (1–2) (2003) 52–56.
[83] A.C. Ferrari, J. Robertson, Origin of the 1150-cm(-1) Raman mode in nanocrystalline diamond, Phys. Rev. B 63 (12) (2001).
[84] J. Schwan, et al., Raman spectroscopy on amorphous carbon films, J. Appl. Phys. 80 (1) (1996) 440–447.
[85] S. Fukura, et al., Factors determining the stability, resolution, and precision of a conventional Raman spectrometer, Appl. Spectrosc. 60 (8) (2006) 946–950.
[86] G. Speranza, N. Laidani, Measurement of the relative abundance of sp(2) and sp(3) hybridised atoms in carbon based materials by XPS: a critical approach. Part I, Diam. Relat. Mater. 13 (3) (2004) 445–450.
[87] S. Stankovich, et al., Stable aqueous dispersions of graphitic nanoplatelets via the reduction of exfoliated graphite oxide in the presence of poly(sodium 4-styrenesulfonate), J. Mater. Chem. 16 (2) (2006) 155–158.
[88] T.I.T. Okpalugo, et al., High resolution XPS characterization of chemical functionalised MWCNTs and SWCNTs, Carbon 43 (1) (2005) 153–161.
[89] J. Filik, et al., XPS and laser Raman analysis of hydrogenated amorphous carbon films, Diam. Relat. Mater. 12 (3–7) (2003) 974–978.
[90] N. Swami, H. He, B.E. Koel, Polymerization and decomposition of C-60 on Pt(111) surfaces, Phys. Rev. B 59 (12) (1999) 8283–8291.
[91] S. Park, et al., Aqueous suspension and characterization of chemically modified graphene sheets, Chem. Mater. 20 (21) (2008) 6592–6594.
[92] C. Mattevi, et al., Evolution of electrical, chemical, and structural properties of transparent and conducting chemically derived graphene thin films, Adv. Funct. Mater. 19 (16) (2009) 2577–2583.
[93] G. Speranza, N. Laidani, Measurement of the relative abundance of sp(2) and sp(3) hybridised atoms in carbon based materials by XPS: a critical approach. Part II, Diam. Relat. Mater. 13 (3) (2004) 451–458.
[94] S.F. Pei, H.M. Cheng, The reduction of graphene oxide, Carbon 50 (9) (2012) 3210–3228.
[95] Y.P. Zhang, C.X. Pan, TiO_2/graphene composite from thermal reaction of graphene oxide and its photocatalytic activity in visible light, J. Mater. Sci. 46 (8) (2011) 2622–2626.

[96] H.A. Becerril, et al., Evaluation of solution-processed reduced graphene oxide films as transparent conductors, ACS Nano 2 (3) (2008) 463–470.
[97] Y. Kawabata, J. Taniguchi, I. Miyamoto, XPS studies on damage evaluation of single-crystal diamond chips processed with ion beam etching and reactive ion beam assisted chemical etching, Diam. Relat. Mater. 13 (1) (2004) 93–98.
[98] R. Sharma, et al., Effect of substrate bias on SE, XPS and XAES studies of diamond-like carbon films deposited by saddle field fast atom beam source, Appl. Surf. Sci. 220 (1–4) (2003) 313–320.
[99] H.R. Karfunkel, T. Dressler, New hypothetical carbon allotropes of remarkable stability estimated by modified neglect of diatomic overlap solid-state self-consistent field computations, J. Am. Chem. Soc. 114 (7) (1992) 2285–2288.
[100] A.T. Balaban, D.J. Klein, C.A. Folden, Diamond graphite hybrids, Chem. Phys. Lett. 217 (3) (1994) 266–270.
[101] K. Umemoto, et al., Carbon foam: spanning the phase space between graphite and diamond, Phys. Rev. B 64 (19) (2001).
[102] K. Haubner, et al., The route to functional graphene oxide, Chemphyschem 11 (10) (2010) 2131–2139.
[103] F.C. Tai, et al., Correlation between I-D/I-G ratio from visible Raman spectra and sp(2)/sp(3) ratio from XPS spectra of annealed hydrogenated DLC film, Mater. Trans. 47 (7) (2006) 1847–1852.
[104] A. Kaniyoor, et al., Wrinkled graphenes: a study on the effects of synthesis parameters on exfoliation-reduction of graphite oxide, J. Phys. Chem. C 115 (36) (2011) 17660–17669.
[105] C. Moreno-Castilla, M.V. Lopez-Ramon, F. Carrasco-Marin, Changes in surface chemistry of activated carbons by wet oxidation, Carbon 38 (14) (2000) 1995–2001.
[106] E.A. Belenkov, V.A. Greshnyakov, Classification schemes for carbon phases and nanostructures, New Carbon Mater. 28 (4) (2013) 273–283.
[107] J.G. Buijnsters, et al., Direct spectroscopic evidence of self-formed C(60) inclusions in fullerenelike hydrogenated carbon films, Appl. Phys. Lett. 92 (14) (2008).
[108] S. Talapatra, et al., Irradiation-induced magnetism in carbon nanostructures, Phys. Rev. Lett. 95 (9) (2005).
[109] J.L. Hueso, et al., XPS investigation of the reaction of carbon with NO, O-2, N-2 and H_2O plasmas, Carbon 45 (1) (2007) 89–96.
[110] A. Siokou, et al., Surface refinement and electronic properties of graphene layers grown on copper substrate: an XPS, UPS and EELS study, Appl. Surf. Sci. 257 (23) (2011) 9785–9790.
[111] D. Yang, et al., Chemical analysis of graphene oxide films after heat and chemical treatments by X-ray photoelectron and Micro-Raman spectroscopy, Carbon 47 (1) (2009) 145–152.
[112] S. Biniak, A. Swiatkowski, M. Pakula, Electrochemical studies of phenomena at active carbon-electrolyte solution interfaces, in: L.R. Radovic (Ed.), Chemistry and Physics of Carbon, Vol. 27, 2001, pp. 125–225.
[113] H. Terrones, M. Terrones, Curved nanostructured materials, New J. Phys. 5 (2003).
[114] K. Xue, Z.P. Xu, Strain effects on basal-plane hydrogenation of graphene: a first-principles study, Appl. Phys. Lett. 96 (6) (2010).